Geomorphology 493 (2026) 110072

Contents lists available at ScienceDirect

Geomorphology

journal homepage: www.journals.elsevier.com/geomorphology

Current flow in low-energy coral forereef spurs and grooves

Lachlan Perris[a,b,*], Tristan Salles[a,b], Thomas E. Fellowes[a,b,e], Ana Paula Da Silva[a,b], Stephanie Duce[b,d], Jody M. Webster[a,b], Alisha M. Thompson[c], Ana Vila-Concejo[a,b]

[a] Geocoastal Research Group, School of Geosciences, The University of Sydney, NSW, 2006, Australia
[b] Marine Studies Institute, Faculty of Science, The University of Sydney, NSW, 2006, Australia
[c] Wenona School, North Sydney, NSW, 2060, Australia
[d] College of Science and Engineering, James Cook University, Bebegu Yumba Campus, Townsville, Queensland, 4811, Australia
[e] Water Research Laboratory, School of Civil and Environmental Engineering, UNSW Sydney, Australia

A B S T R A C T

Coral forereef hydrodynamics, driven by waves and currents, play a critical role in controlling the distribution of nutrients, sediments and corals across platform reefs. These processes drive the formation of reef systems and are critical to determining the future of coral reef environments in a changing global climate. Despite this, limited *in-situ* research from the Great Barrier Reef (GBR) into the interactions between spurs and grooves (SaG) and forereefs currents is available. Here we analyse the first dataset of current measurements from a coral forereef SaG system in the GBR and assess forereef currents adjacent to a large reef lagoon that is isolated from the open ocean during low tides. We find that under prevailing weather conditions, waves are low (Hs = 0.25 m) and oblique to forereef isobaths. Currents in SaG under low wave exposure exhibit high velocity (2 m/s) with a dominant offshore component driven by surf zone processes and lagoonal outflow. This is consistent with postulated mechanisms of constructional development of SaG whereby offshore flow transports sediments seaward of the forereef, providing a substrate for coral larvae and living coral fragments to attach. These *in-situ* observations provide the first evidence from the GBR linking prevalent hydrodynamic conditions to the morphological evolution of coral forereef spur and groove systems.

1. Introduction

Hydrodynamic forcings dictate the transport and availability of sediments and nutrients therefore controlling all aspects of life on coral reef systems (Odum and Odum, 1955) across all spatial and temporal scales (Monismith, 2007). The outer forereef of platform reefs serves as the interface between open ocean hydrodynamics and the reef processes (Munk and Sargent, 1948). Consequently, on undisturbed platform reef systems, lagoon systems fill and drain based on the interplay of tides, waves and currents around the reef rim. This dynamic, in turn, is influenced by the morphology of the forereef and reef flat (Grimaldi et al., 2022; Lowe and Falter, 2015). The feedback between hydrodynamics and morphology across these reef zones offers valuable insights into the long-term geomorphic evolution of coral reefs.

In this study, we investigate a ubiquitous, yet under-studied, morphological feature of forereefs known as spurs and grooves (SaG). Spurs are elongate finger-shaped formations of carbonate material that stretch seaward from the reef flat. Grooves are channels or troughs that intermittently separate the spurs (Duce et al., 2016; Munk and Sargent, 1948). SaG have been documented across different reef types including platform reefs, fringing reefs, barrier reefs and atolls, with SaG morphology varying considerably in response to local conditions (Cloud, 1959; Duce et al., 2014). They have been observed through all coral-rich seas including the Red Sea (Sneh and Friedman, 1980), the Atlantic Ocean (Shinn, 1963), the Indian Ocean (Sheppard, 1981; Weydert, 1979), the Caribbean Sea (Blanchon and Jones, 1997; Goreau, 1959), and the Pacific Ocean (Munk and Sargent, 1948; Storlazzi et al., 2003). Despite comprehensive documentation of SaG presence, *in-situ* measurements of current regimes in platform reef SaG systems are scarce. This paucity of hydrodynamic field measurements is likely due to the challenging turbulent surf zones of forereefs where SaG typically develop (Duce et al., 2020, 2014; Munk and Sargent, 1948), making access difficult.

Remotely sensed data has provided the greatest insight into SaG morphology to date, with four classes of SaG defined in the Southern Great Barrier Reef based on morphometrics and relative exposure to wave energy (Fig. 1) (Duce et al., 2016). Numerical modelling over remote-sensed SaG bathymetries has demonstrated that grooves of different classes exhibit distinct hydrodynamic regimes (Perris et al., 2024). Consequently, accounting for SaG morphological classifications is essential in any hydrodynamic analysis involving these systems.

Early reports of waves in SaG zones by Munk and Sargent (1948)

* Corresponding author at: Geocoastal Research Group, School of Geosciences, The University of Sydney, NSW, 2006, Australia.
E-mail address: lachlan.perris@sydney.edu.au (L. Perris).

https://doi.org/10.1016/j.geomorph.2025.110072
Received 15 June 2025; Received in revised form 12 October 2025; Accepted 19 October 2025
Available online 22 October 2025
0169-555X/

Munk and Sargent (1948) at Bikini Atoll, Republic of the Marshall Islands, inferred a relationship between wave direction and the orientation of forereef grooves. This was later supported by Sneh and Friedman (1980) Sneh and Friedman (1980) in the Red Sea with SaG perpendicular to refracted waves. This has led to numerical modelling efforts that consider waves perpendicular to the primary groove axis (da Silva et al., 2020; Perris et al., 2024; Rogers et al., 2013). In nature, exposed platform reefs can receive incident waves from a wide range of directions depending on the offshore wave parameters, fetch distance and refraction/diffraction around the reef. SaG in low-energy regions differ morphologically from their high-energy counterparts (Duce et al. (2016), modified in Fig. 1), leaving a gap in our understanding of how these systems persist under predominantly low-energy and oblique wave settings.

Direct measurements of currents in SaG have only been reported in five reefs worldwide: Molokai in Hawaii (Storlazzi et al., 2004), Moorea in French Polynesia (Rogers et al., 2013), Palmyra Atoll in the central Pacific (Rogers et al., 2015), at Xahauyxol Reef in the Mexican Caribbean (Acevedo-Ramirez et al., 2021) and Ngederrak reef in Palau, Western Pacific (Sartori et al., 2024). Notably, to our knowledge no current measurements have ever been published from SaG in the Great Barrier Reef (GBR). Of the studied reefs, Molokai and Xanhauyxol are fringing reefs, and Moorea is a barrier reef—each exhibiting hydrodynamic regimes that differ significantly from those of platform reefs. Palmyra atoll has a large engineered navigational channel cut through its forereef and reef flat, which alters lagoon circulation patterns (Gardner et al., 2011) and obfuscates the natural processes of lagoon-seawater exchange. Therefore, additional studies are needed to understand the characteristics of current flows through a platform reef SaG system.

With limited *in-situ* data across the wide range of reef morphologies, numerical models have so far provided the most significant insights into forereef SaG currents. (Rogers et al., 2013) proposed that SaG induce counter-rotating Lagrangian circulation cells by creating alongshore variations in depth and friction. This concept was further expanded upon by da Silva et al. (2020), who used a comprehensive set of numerical models over idealised SaG bathymetry to identify vertical Lagrangian circulation cells under various wave conditions and water levels. Across all simulations, currents within the groove were directed onshore. However, in low-wave energy SaG, there is a relative reduction on the role of wave induced currents compared to the effects of high tidal ranges and reef lagoon outflow. Lagoon waters experience greater temperature fluctuations and increased salinity due to evaporation when isolated from the comparatively fresh water of the surrounding ocean (Silverman et al., 2012). The mixing of lagoonal and ocean waters around the forereef are critical to coral health in these regions. Numerical models have shown that lagoon waters can enter the open ocean *via* undertows over the forereef (Lindhart, 2022). Since grooves represent local bathymetric minima, they may serve as pathways for lagoonal outflow, potentially influencing longer term SaG morphological evolution. Yet, there has been no published investigation into the role of SaG morphologies in mediating lagoon-to-ocean exchanges, leaving a significant gap in the understanding of these processes.

Flows at forereef SaG are essential to understanding the mechanisms driving their formation. A comprehensive short-coring analysis of vertical and lateral progradation rates on coral forereefs in the southern GBR demonstrated three modes of SaG development (Duce et al., 2020). *Mode 1* occurs in wave dominated environments, where erosion of the forereef likely exceeds accretion. In this mode, both the reef flat and the SaG were prograding toward the lagoon. *Mode 2* develops in moderate or episodic wave energy environments, where SaG potentially develop over antecedent bathymetry featuring proto-spurs. And finally, *Mode 3* arises in low wave energy conditions, providing a mechanism for the seaward accretion of both the reef flat and the forereef. In *Mode 3*, offshore flows from the lagoon supply reef sediments to the outer forereef, with reduced wave energy increasing sediment residency time. This creates a substrate conducive to the seaward accretion of the forereef and reef flat. This aligns with findings that relative wave energy influences the direction of reef flat lateral accretion (Dechnik et al., 2016), including oceanward accretion in lower hydrodynamic settings. These three modes offer a framework for understanding how varying hydrodynamic and sedimentary conditions drive SaG formation and contribute to reef platform evolution. While this model of SaG formation relies on an interpretation of hydrodynamics in a SaG system, it was not based on *in-situ* hydrodynamic measurements of current, which have never been reported from the GBR.

This study addresses three key gaps in understanding the hydrodynamics of spur and groove systems in low-energy reef settings: (1) Can spurs and grooves persist under prevalent oblique wave conditions? (2) What are the characteristics of current flows in these systems under such conditions? and (3) Do the observed hydrodynamics support a constructional model of SaG formation and reef platform evolution?

2. Materials and methods

2.1. Study site

One Tree Reef (OTR) (23°30′S, 152°06′E) is a lagoonal platform reef located 84 km offshore in the southern Great Barrier Reef (GBR) (Fig. 3). It benefits from limited anthropogenic impacts and is protected within

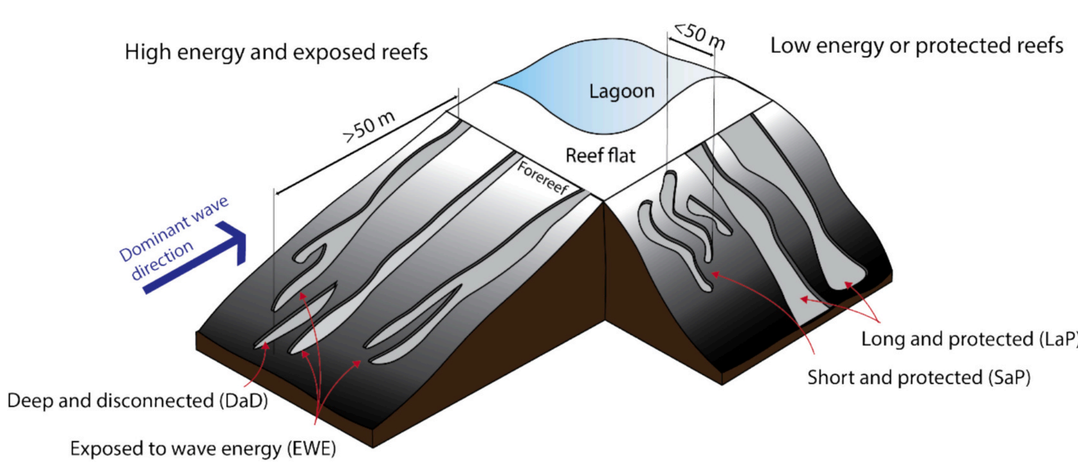

Fig. 1. A schematic of SaG morphotypes modified after (Duce et al., 2016). High energy SaG morphotypes, 'Exposed to wave energy' and 'Deep and Disconnected' face the dominant wave direction (blue arrow), bifurcation of 'exposed to wave energy' grooves is common. Low energy morphotypes, 'short and protected' and 'long and protected', typically occur in less exposed areas of a reef, such as the area being investigated here.

the GBR Marine Park's "Scientific Zone." OTR experiences semi-diurnal tides, with a mean spring tidal range of 3 m. Offshore hydrodynamics at OTR are primarily influenced by southeast trade winds of the Coral Sea, which dominate over 70 % of the year (Jell and Webb, 2012). These winds result in an average significant wave height of 1.7 m (Smith et al., 2023). Periodically, the reef is impacted by extreme waves conditions associated with tropical storms and cyclones, during which significant wave heights exceed 3 m (Smith et al., 2023).

The reef crest at OTR is unbroken by channels, isolating lagoonal waters from the open ocean for 6 h of the tidal cycle—a phenomenon known as tidal truncation (Silverman et al., 2012). During this period, the water level inside the lagoon can be up to 0.2 m higher than the surrounding ocean, and the maximum water level within the lagoon can exceed that of the external tide due to wave forcing around the reef (Wilson, 1985). Prevailing E–SE swells push water onto the reef flat and into the lagoon, a process known as wave pumping, where waves on the exposed reef and wind shear over the lagoon drive water across the reef platform. This water subsequently drains on the leeward side of the reef, producing lagoon outflows that are commonly focussed at local topographic low points (Frith and Mason, 1986). OTR is entirely encircled by SaG (Duce et al., 2016), with this study focusing on a SaG system on the northern forereef (Fig. 3). Here, the reef flat is exposed for 3 h during the tidal cycle, while adjacent upper forereef spurs are exposed only during the lowest astronomical tides. The spurs show high coral cover and surface roughness, indicative of a healthy reef (Harris et al., 2023), while groove beds are filled with coarse and rounded rubble. About 300 m west of the study site is "The Entrance," a low point in the reef crest that roughly corresponds to the half-tide level (Wilson, 1985) and provides vessel access for about 3 h during each high tide (Ludington, 1979). A prominent storm-deposited rubble bank lies across the reef flat (Fig. 3), measuring approximately 350 m in length and 30 m in width. This feature reflects onshore transport of coral rubble during periodic storm-driven erosion of the adjacent forereef (Davies, 1983). Its presence indicates that large volumes of sediment can be stored temporarily on the reef flat following high energy events, providing a potential source of material that may under high-energy conditions be transported seaward and channelled by strong offshore currents through the groove.

2.2. Morphology

Morphological measurements of the coral forereef were derived from a 0.25 m × 0.25 m resolution airborne LiDAR digital elevation model (Fig. 3) (Harris et al., 2023). SaG features were identified and classified according to the Duce et al. (2016) scheme (Fig. 1). The following metrics were then computed for each SaG element: Spur height (h_{spur}) vertical distance from the groove floor to the crest of the adjacent spur. Groove length (L): the centre-line path length measured along the groove axis. Groove sinuosity (S): the ratio of straight-line distance (x) between groove endpoints to the path length L (*i.e.* $S = x/L$). Mean slope (θ): the average inclination of each spur or groove segment, calculated as the arctangent of elevation change over the horizontal extent. All measurements were extracted in GIS software (ArcGIS Pro v3.1). Elevations were referenced to mean sea level based on the AUSGeoid 2009 offset of the Australia Height Datum (Featherstone et al., 2011). Spur and groove endpoints were manually inspected to ensure correct feature pairing (Fig. 2).

2.3. Instrument deployments

We collected field data of waves and currents between 06/10/2022 and 08/10/2022 along a cross-shore transect in a forereef groove (Fig. 3, Table 1). Two Nortek Vectors (A1 and A2) and an RBR Virtuoso[3] pressure transducer (P1) were deployed, sampling continuously at 8 Hz. Nortek vectors (A1 and A2) include integrated inertial motion units which were calibrated in the deployment frame and clear of any other

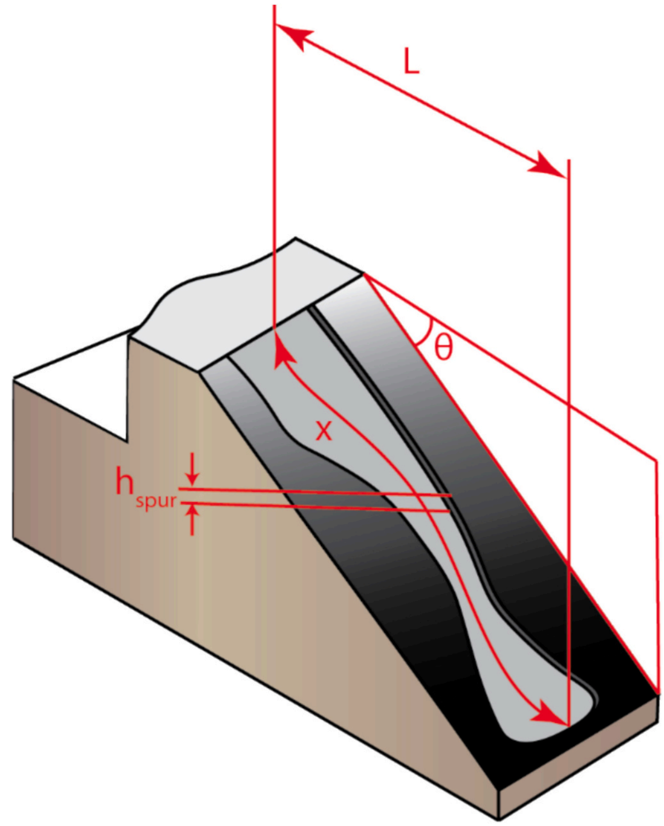

Fig. 2. Schematic of a single groove with relevant dimensions, Spur height (h_{spur}) vertical distance from the groove floor to the crest of the adjacent spur, Groove length (L): the centre-line path length measured along the groove axis. Straight-line distance (x) between groove endpoints and mean slope (θ): the average inclination of the spur (shown in red) is also calculated for the groove bed.

metallic disturbances, to remove any potential errors due to the presence of metals influencing the magnetic field. Additionally, data was recorded in XYZ coordinates which are based on the positioning of the instrument, rather than compass bearings. We aligned both A1 and A2 with the groove, so that the x-direction aligned with the western groove wall. By including both measurements (inertial motion unit and XYZ) we were able to determine any errors in the alignment of the instrument with compass bearings. We determined the mean deployment depth (Table 1) from pressure readings at each instrument. We measured the distance of each instrument from the reef crest, defined as the mean sea level contour derived from the LiDAR digital elevation model (Harris et al., 2023) and referenced to Australian Height Datum (AHD) using the AusGEOID09 model (Featherstone et al., 2011) (Table 1).

A second survey was conducted between 31/10/2023 and 27/03/2024 to assess hydrodynamic connectivity between the lagoon and the open ocean, as well as to provide an indication of representative offshore wave parameters at the study site. This array included a Sofar Spotter Buoy and Smart Mooring with a near-bed mounted RBR conda[3], measuring temperature and pressure (B1, Table 1). To place both surveys in a broader seasonal context, conditions measured at B1 were compared with those from the first survey, together with local wind speed and direction obtained from the open-meteo API (Zippenfenig, 2023) and offshore wave conditions derived from satellite radar-altimeter data using the RADWave Python package (Smith et al., 2020).

2.4. Local weather conditions

Local wind speed and direction during the deployment were derived

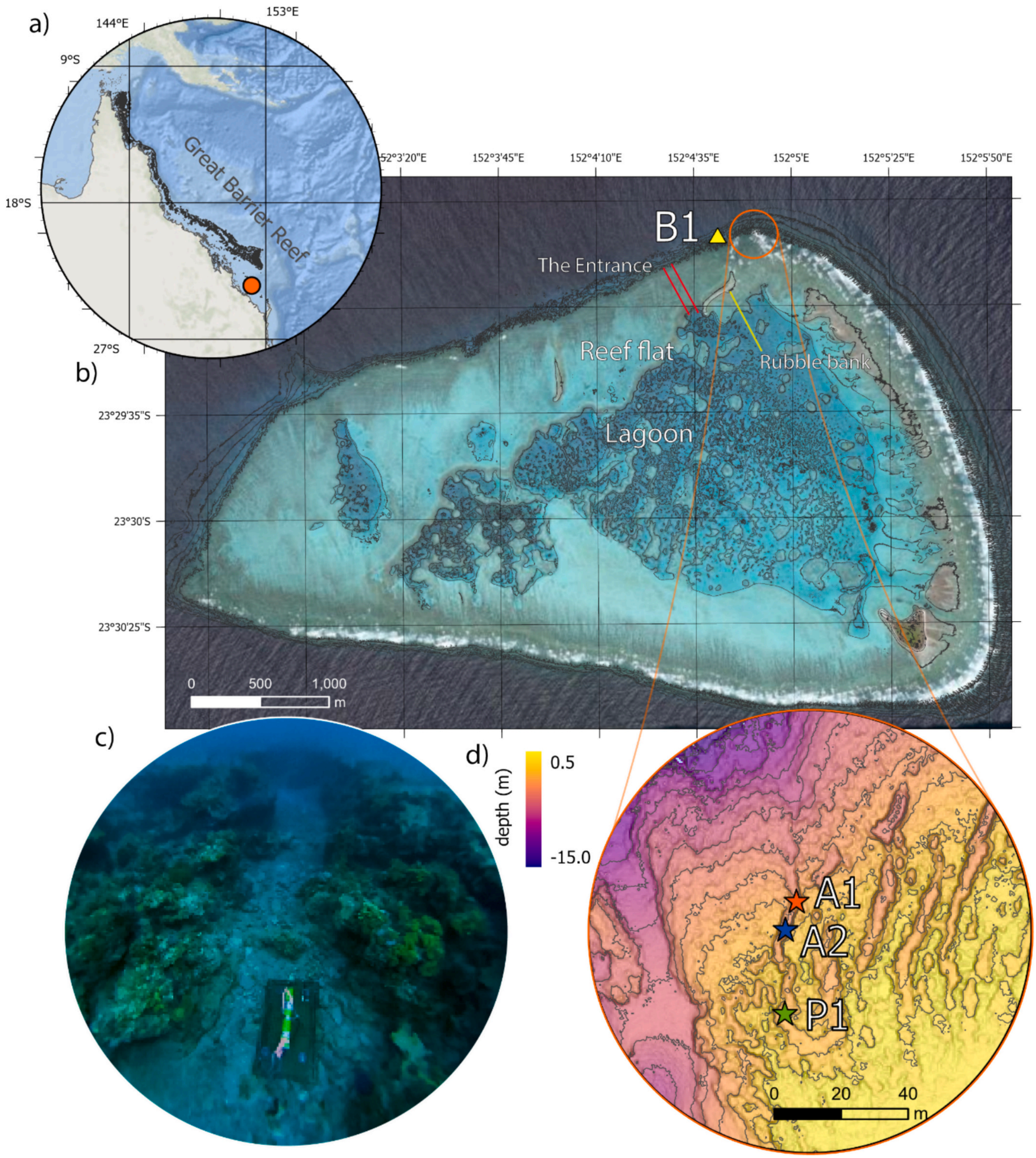

Fig. 3. a) One Tree Reef (OTR) is in the southern Great Barrier Reef (orange circle). b) Study site and location of Spotter wave rider buoy (B1), the study site is located on the northern forereef of OTR, 400 m from '*The Entrance*' (shown with red lines), the yellow line indicates the location of a storm-deposited rubble bank c) instrument A1 in place within a groove and, d) the location of the instruments in that groove, A1 and A2 are Nortek Velocimeters and P1 an RBR Virtuoso pressure transducer (Table 1).

from open-meteo API (Zippenfenig, 2023). Offshore wave conditions were extracted from satellite radar-altimeter measurements using the RADWave Python package (Smith et al., 2020). RADWave (v 1.0.8) interfaces directly with THREDDS data services to access the Australian Ocean Data Network global altimeter archive (Ribal and Young, 2019). Within our workflow, we specified a bounding-box region east of OTI from latitude 22°S to 25°S and longitude 152.1°E to 156°E, then retrieved along-track measurements of sea surface elevation. RADWave subsequently computes standard wave parameters—significant wave height (H_s), peak period (T_p). Local weather conditions during the

Table 1
Instrument deployment details.

Name	Deployment period	Instrument	Sample rate (Hz)	Mean deployment depth (m)	Distance from bed (m)	Distance from crest (m)
A1	06/10/2022–08/10/2022	Nortek Vector	8	3.6	0.12	100.2
A2	06/10/2022–08/10/2022	Nortek Vector	8	3.3	0.24	92.4
P1	06/10/2022–08/10/2022	RBR Virtuoso	8	2.4	0.15	66.6
B1	31/10/2023–27/03/2024	Sofar Spotter Buoy with Smart Mooring (RBR Conda3)	3.84	10.5	1.5 (RBRConda 3), 10.5 (Spotter Buoy)	97

deployments (Table 1) were compared across surveys and against mean conditions for OTI.

2.5. Data processing

Field data of three-dimensional current vectors (recovered from the current meters A1 and A2) were processed using the Doppler Oceanography Library for Python (DOLfYN) (Klise et al., 2020). To remove spikes caused by Doppler noise, aliasing of the Doppler signal or boundary interference, we implemented a phase-space threshold despiking algorithm (Goring and Nikora, 2002). A block size of $npt = 5000$ points was employed throughout. Long runs of missing data ($\geq npt/10 = 500$ points) were first identified and used to segment the time series so that each continuous "good" interval was processed independently. Within each block of 5000 samples, spikes were iteratively flagged if their velocity–derivative pair lay outside the expected phase-space envelope. Iteration continued until no additional spikes were detected (or a maximum of 100 cycles was reached). The resulting Boolean mask marked all despiked points, which were then omitted from further analysis.

Current meters A1 and A2 were deployed in alignment with the groove such that the positive x-direction was directed toward the western groove wall. Cross-shore and alongshore directions were defined based on the orientation of isobaths and the reef crest. Mean current directions were determined *via* circular mean calculations for each tidal phase (low and high). Tide induced currents were separated from wave induced currents by temporally averaging the time series at three-hour intervals.

2.5.1. Wave data analysis

Wave data was processed for pressure sensors on all three instruments (A1, A2 and P1) (Fig. 3c). We analysed raw pressure data with zero-crossing methods following (Karimpour and Chen, 2017) (see Data Availability). We calculated wave parameters of significant wave height (H_s) and peak wave period (T_p) using linear wave theory —an approach validated on steep and complex coral reef bathymetries (Monismith et al., 2013). We used spectral analysis in 15-minute intervals, that was found to be appropriate for long wave lengths at OTR (Harris et al., 2015). The one-sided bottom pressure spectrum is given by:

$$p_x(f_k) = 2\,\frac{\Delta t}{n}|X_k|^2 \tag{1}$$

And only the spectral bin for all waves satisfying $0.0033 \leq f_k < 2.0$ Hz are retained. We then calculated the zeroth moment m_0 such that:

$$m_0 = \sum_k S_\eta(f_k)\Delta f \tag{2}$$

where $\Delta f = \frac{1}{n}\Delta t$ for an $n-point$ record at sampling frequency (Δt) and $S_\eta(f_k)$ is the power spectral density of the surface elevation of frequency (f_k). Under linear wave theory, Hs is related to the zeroth moment (m_0) by:

$$H_s = 4\sqrt{m_0} \tag{3}$$

We calculated the peak period T_p such that:

$$T_p = \frac{1}{f_p} \tag{4}$$

where f_p is the maximum of the spectral density $(p_x(f_k))$. Wave power was calculated using linear wave theory:

$$P = C_g E \tag{5}$$

where E is the wave energy density and c_g is the group speed determined for intermediate depths, such that:

$$c_g = \frac{c}{2}\left(1 + 2\frac{kh}{sinh2kh}\right) \tag{6}$$

where c is the phase velocity, h is the water depth, and the wave number (k) and wave celerity (c) were derived using the Newton-Raphson method for the dispersion relation (Dean and Dalrymple, 1991). To investigate wave breaking over the instruments, we calculated:

$$\gamma = \frac{H_{max}}{h} \tag{7}$$

where H_{max} is derived from spectral analysis of the water elevation time series, and γ is the wave breaking parameter. Values for γ have been published for forereef environments varying from 0.83 (Rogers et al., 2016) and 0.98 (Monismith et al., 2013). We used a conservative estimate of $\gamma = 0.60$ to ensure that no waves were breaking over the instruments, as has been demonstrated on forereefs in a similar study (Duce et al., 2021). Finally, we did not compute dissipation rates and reflection coefficients because of the oblique nature of incident waves.

2.5.2. Temperature data analysis

To further investigate the origin of currents in the forereef and determine the mean wave conditions at the study site, a secondary analysis was conducted with the Spotter Buoy (B1) and a near-bed mounted sensor (Table 1). The temperature gradient was calculated as the difference between the buoy-mounted temperature logger and the near-bed mounted temperature logger, with water depth measured by the co-located pressure sensor. A temperature inversion was identified when the water temperature at the bed was higher than at the surface. Spectral and time domain analyses were performed on displacement data collected by the wave buoy, following (Kinsela et al., 2024).

3. Results

3.1. Morphology

The study area (Fig. 3) features SaG of varying morphologies. Following the morphological classification system of Duce et al. (2016) (Fig. 1), we identified 'short and protected' grooves, which are located west of the study site in an area with lower exposure to the dominant south-easterly swell, and 'deep and disconnected' grooves on the lower forereef slope at the study site. The groove investigated here belongs to the 'long and protected' class (Fig. 1), measuring 79 m in length, with a mean width of 5 m and a spur wall height reaching up to 2.2 m above the groove bed. Field observations show that spur walls overhang the groove, meaning that the groove width at the bed may be underestimated due to the constant scanning height and angle of airborne LiDAR. Due to this constraint, it is only possible to identify where spurs overhang grooves from *in situ* observations. In an analysis of 11,430 grooves across 17 reefs in the Southern GBR, including this study site, OTI, Duce et al. (2016) showed that overhanging spur walls are more common on 'long and protected' or 'short and protected' groove classes which represent 42 % of 11,430 surveyed grooves (Duce et al., 2016). Groove sinuosity – the ratio of straight-line distance to path length – is 0.91. The forereef slope is consistent between the groove and the spurs, at 1.8°. Mean spur wall height adjacent to each instrument is 2.1 m.

3.2. Local weather conditions

A mean offshore wave height of 1.75 m was determined for the deployment period. Mean offshore wave heights at OTR were 1.7 m from 1985 to 2018 (Smith et al., 2023) (Fig. 4 a). Consequently, the conditions measured in this analysis represent the prevalent wave conditions of OTR. The mean wind condition during the study period was 5.74 m/s from 92°N (easterly winds). Mean H_s at instrument B1 (Table 1) was 0.6 m with a mean wind speed of 4.2 m/s from 107°N (east-south-easterly winds).

3.3. Wave analysis

The deployment encompassed three full tidal cycles with an average tidal range of 2.41 m (Fig. 5a). The principal axis of flow for instruments A1 (furthest offshore) and A2 was found to be 93° and 61° respectively, indicating mostly oblique waves at the offshore instrument that refract toward the reef crest at instrument A2. The mean H_s at instrument A1 (farthest offshore) was 0.24 m (Fig. 5b), indicating a significant reduction in wave height occurred before reaching the survey site. Mean H_s at instrument A2 was the lowest at 0.21 m (Fig. 5c).

The H_s at instrument P1, closest to the reef crest, were controlled by water level (0.87 Pearson correlation), with mean H_s ranging from 0.16 m at low tide to 0.25 m at high tides (Fig. 5d). The analysis of wave breaking determined that waves were not breaking above any of the instruments, despite a conservative estimate of the wave breaking threshold, $\gamma = 0.6$ (Eq. (7)).

Wave power (P) at each instrument were controlled by tidal cycles with higher wave power observed during high tides. At instrument P1, the mean wave power at high tide was 166 % greater than at low tides. At instrument A1 and A2, this increase was 59 % and 40 % respectively (Table 2). The influence of water level on wave power was most pronounced at instrument P1, located closest to the reef crest, where the Pearson correlation between intermediate wave power and water level was 0.92. At site A1 (furthest from the reef crest) the correlation was 0.86, and at site A2, it was 0.65.

3.4. Current analysis

We quantified the maximum and mean velocities at each instrument. Measurements are taken as a point measurement sufficient to describe currents in the forereef groove, importantly, we do not extrapolate these results to the above water column. At instrument A1, the maximum current velocity was 2.25 m/s, directed at 150°N (offshore and to the west), with maximum offshore and onshore current velocity of 1.94 m/s and 2.06 m/s, respectively (Figs. 7b and 8a). The mean absolute velocity magnitude at instrument A1 was 0.12 m/s (Fig. 6d), and the mean cross-shore current velocity was directed offshore at 0.04 m/s (Fig. 6b). This cross-shore current decreased to 0 m/s at high tides but increased to 0.07 m/s offshore at low tide (Fig. 6b).

Flow velocities were higher at the nearshore instrument, A2, with a maximum current velocity of 2.87 m/s directed at 39.8°N (offshore and to the east). At A2 we recorded maximum offshore and onshore velocity components of 2.05 m/s and 1.45 m/s, respectively (Fig. 7c and b). The mean velocity magnitude measured at instrument A2 was 0.17 m/s, with the mean cross-shore current velocity indicating mean offshore current of 0.12 m/s (Fig. 7c). This offshore current was consistent across the full tidal cycle, with values decreasing to 0.03 m/s at high tide and increasing to 0.18 m/s during low tide (Fig. 6c). Isolated peaks in cross-shore directed velocity were recorded during low tides (Fig. 7b); we interpret this as likely caused by a short-term wave-breaking jet or localised flow convergence, rather than representing the prevailing flow regime. We attribute the observed variation in offshore flow to tidal modulation of lagoon connectivity. At high tide, the lagoon is more hydrodynamically open to the surrounding ocean, reducing the pressure gradient that drives outflow and thereby limiting offshore-directed currents. As the tide falls, the lagoon becomes increasingly truncated from the open ocean and offshore flow from the lagoon increases due to higher water levels in the ponded lagoon. This generates stronger

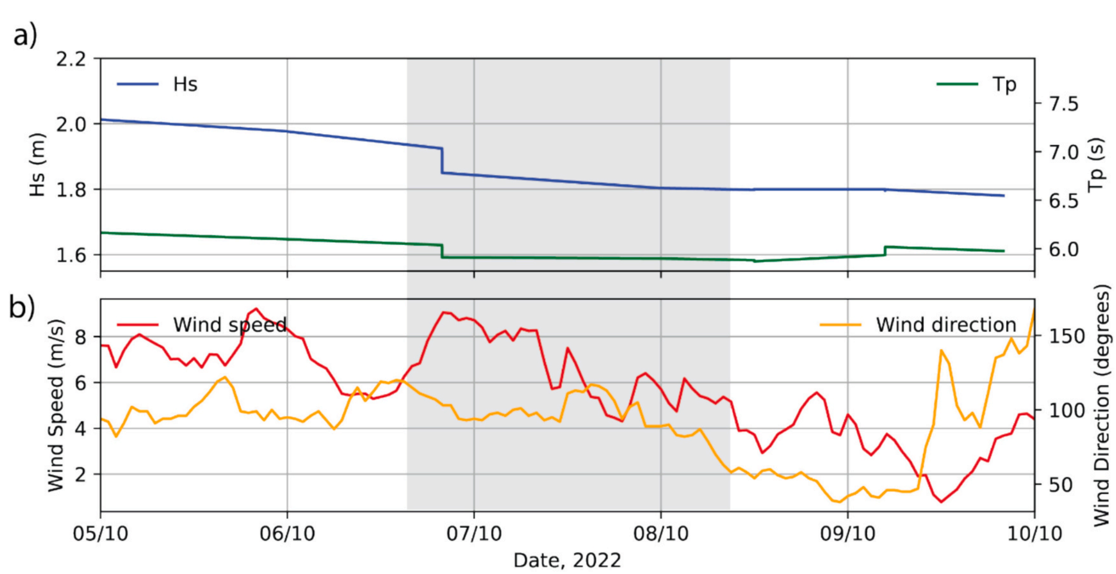

Fig. 4. a) Offshore H_s (left y-axis) and T_p (right y-axis) derived from satellite altimetry (Smith et al., 2020), and b) wind speed (left y-axis) and direction (right y-axis) for the deployment period in October 2022 (highlighted in grey) (Zippenfenig, 2023).

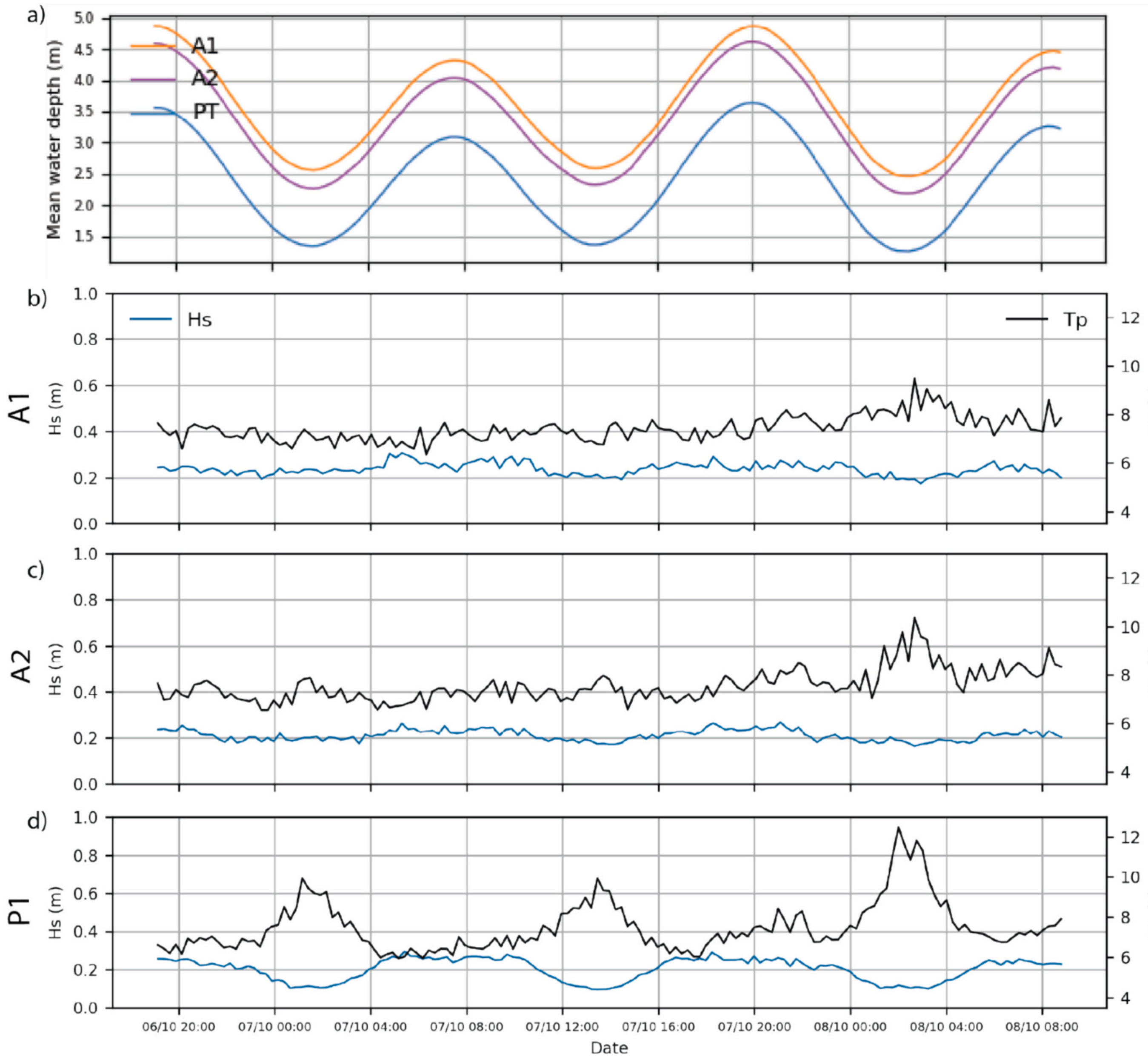

Fig. 5. Hydrodynamic measurements from 6 to 8 October 2022. (a) Mean water depth at each instrument (b, c, and d) present the H_s and T_p at A1, A2 and P1 respectively, from the most offshore to the most shoreward instrument.

Table 2
Wave parameters averaged over the tidal period (high or low tide).

Instrument	$\overline{H_{s\ low\ tide}}$ (m)	$\overline{P_{low\ tide}}$ (W/m^2)	$\overline{H_{s\ high\ tide}}$ (m)	$\overline{P_{high\ tide}}$ (W/m^2)
P1	0.16	130	0.25	346
A2	0.19	208	0.23	331
A1	0.23	283	0.25	398

offshore flows through the groove during low tide conditions.

3.4.1. *Current velocity and tidal controlled water levels*

Current velocities within the grooves increased markedly during falling tides; however, the relationship with water level was non-linear. At instrument A1, a pronounced rise in velocity was observed when the water level dropped below 2.9 m (mean depth: 3.6 m), and at A2 when it fell below 2.6 m (mean depth: 3.3 m) (Fig. 7). At these thresholds, water depths over the adjacent spurs were reduced to 0.4 m and 0.6 m, respectively. Importantly, at A2, the onset of increased current coincided with wave breaking on the adjacent spurs, which occurred once water depth fell below the estimated breaker depth (using a conservative $\gamma = 0.6$). In contrast, no breaking was observed within the deeper grooves at this stage of the tidal cycle. These observations suggest that wave breaking on spurs during low tide enhances along-groove currents, likely due to the lateral redirection of wave-driven momentum.

The circular mean current direction at instrument A1 was 359.8°N, and at instrument A2, it was 346.5°N. In both cases, the mean current direction was offshore (Fig. 8). As water level increased, current direction became less constrained to the groove (Fig. 8) and more oscillatory due to wave motion (Fig. 7 b, c).

3.4.2. *Current direction analysis*

Current direction was consistently offshore across all tidal levels at instrument A2, located nearest to the reef crest ($u_{mean} = 0.11$ m/s). This current was greatest at low tides ($u_{mean,\ low\ tide} = 0.18$ m/s) (Figs. 7, 8).

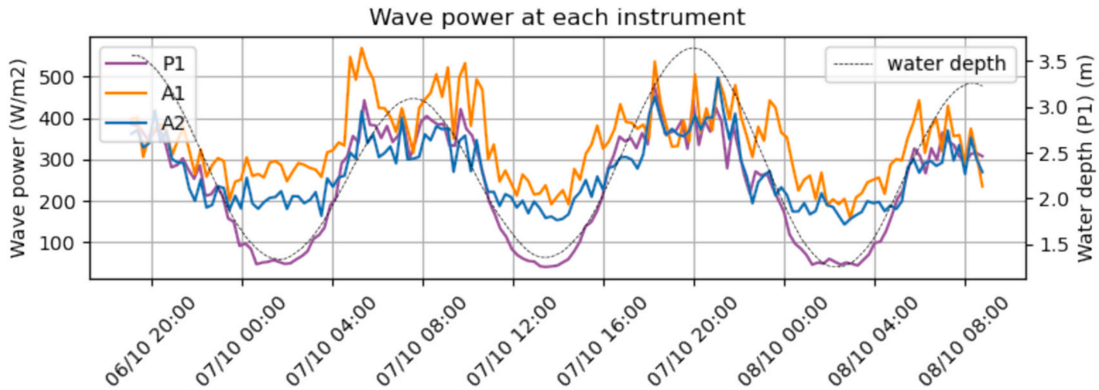

Fig. 6. Wave power calculated at each instrument (A1, A2 and P1) and measured water depth at instrument P1.

Similarly, temperature gradient inversions, with cooler water at the surface and warmer water at the bed, occurred during the second deployment at instrument B1 in phase with tidal cycles (Figs. 8 and 9), inferring the presence of internal waves or density driven flows.

The temperature gradient was inverted for most of the deployment of instrument B1 (69 %), likely due to constant outflow from the lagoon. On average, the mean temperature (26.5 °C) at the seafloor was similar to that at the surface (26.6 °C), but there were considerable oscillations in the temperature difference (ΔT) from the surface to near seafloor. The maximum temperature inversion recorded was 2.06 °C (Fig. 8a).

4. Discussion

4.1. Spurs and grooves can exist under prevailing oblique waves in low-energy settings

Since early observations by Munk and Sargent (1948), SaG systems are often considered to only exist under shore-normal incident high energy waves. Previous studies of SAG have only considered shore-normal waves, both in field observations (Acevedo-Ramirez et al., 2021; Rogers et al., 2013; Storlazzi et al., 2004) and numerical modelling (da Silva et al., 2020; Perris et al., 2023). For example, in a comprehensive numerical model utilising an idealised SaG bathymetry, (da Silva et al., 2020) predicted low magnitude flows in SaG of 0.01–0.1 m/s under wave heights of 0.5–6 m. A field study at Palmyra Atoll with wave conditions of root-mean-square wave height (H_{rms}) between 0.6 and 1.3 m in a microtidal (0.8 m) environment measured weak currents in a groove, up to 0.20 m/s (Rogers et al., 2015) directed offshore on the upper forereef.

However, during this study, we measured low-energy oblique waves ($P = 340.6$ W/m at A1, Fig. 5 b, c) and offshore currents in the grooves likely driven by lagoon outflow (Fig. 9). While we observe a similar direction of flow to that found by Rogers et al. (2015), our observations include substantially higher current velocities of up to 1.45 m/s at the outer station (A1) during low tides, despite a maximum significant wave height of only 0.23 m (P = 340.6 W/m, Fig. 6, Table 2). This is probably related to the enhanced offshore currents due to the outflow of lagoon water, as discussed in Section 4.2.

We did not observe the Lagrangian circulation cells previously modelled under shore-normal waves, where current was offshore over the spurs and onshore in the grooves (da Silva et al., 2020; Rogers et al., 2013). We hypothesise that these circulation cells may emerge when wave power increases and dominates over the lagoon outflow, or when the direction of incoming waves becomes shore-normal and parallel to grooves for example, during tropical cyclone conditions (Woolsey et al., 2012). The studied low-energy SaG therefore exist under prevailing oblique incident waves, and their hydrodynamics are primarily driven by wave pumping and lagoon outflow, leading to offshore currents under prevailing low energy conditions (Fig. 10).

This pattern is similar to currents observed in rip channels on open coast beaches, where shore-connected shoals exhibit higher current velocities compared to the seaward surf zone (MacMahan et al., 2004). However, in our case, given the thermal inversions observed at instrument B1, the offshore current at the inner groove (A2) is more likely driven by tidally induced lagoon outflow than by wave pumping *i.e.* the mass balance of the reef system, rather than surf zone dynamics.

4.2. The groove channelises the outflow of lagoon water during prevailing low-energy wave conditions

We found decreased wave power at low tides (Fig. 6, Table 2), likely due to increased frictional dissipation of waves over the forereef slope. The low wave power conditions and non-shore-normal waves observed in this area had minimal impact on the offshore flows within the groove. We observed greater mean wave power at the outer groove (A1, $P = 283$ W/m) than at the inner groove (A2, $P = 208$ W/m), consistent with linear wave theory, which predicts a reduction in wave energy as waves shoal and dissipate due to bottom friction and breaking over complex and steep forereef bathymetries (Monismith et al., 2013).

Additionally, from temperature inversions offshore of the grooves (instrument B1), we infer that hypersaline lagoon waters are sinking under the surface ocean water. This dense and warm hypersaline lagoon water has been observed in other atoll reef settings, including Palmyra Atoll, which is a larger more open lagoon than our study site (Gardner et al., 2011), and Clipperton Atoll in the Eastern Pacific, which, similar to our study site, has few topographic low points on the reef rim for open ocean and seawater exchange (Jost and Andréfouët, 2006). The offshore currents measured at the study site therefore likely correspond to lagoon outflows of hypersaline warm water that are driven by wave pumping across the lagoon (*sensu* Callaghan et al., 2006) due to the E–SE wave conditions. The lagoon outflow then sinks and travels offshore as bottom currents inside the groove, resulting in the warmer bed temperatures observed seaward of the SaG at B1 (Fig. 9 a, b). While seasonal variability likely influenced wave energy and lagoonal exchange, the mechanisms observed (*e.g.*, lagoon outflow driving offshore currents through grooves) are not dependent on season but on relative tide–wave interactions, consequently, the temperature inversions were measured during in a period of lower wind speed and offshore wave height, which have been proposed to drive currents over the lagoon (Ludington, 1979).

The observations of thermal inversions at the reef rim are consistent with observations of coral bleaching in the One Tree Reef lagoon (Byrne et al., 2025) and on the deep northern forereef during a coral bleaching event in January 2024 (One Tree Island Research Station Managers Personal Communication). While our observations suggest that offshore-directed currents are driven primarily by lagoon outflow, the short deployment window limits the ability to capture longer-term variability, including responses to high-energy events. Future studies should incorporate longer deployments and direct measurements of sediment

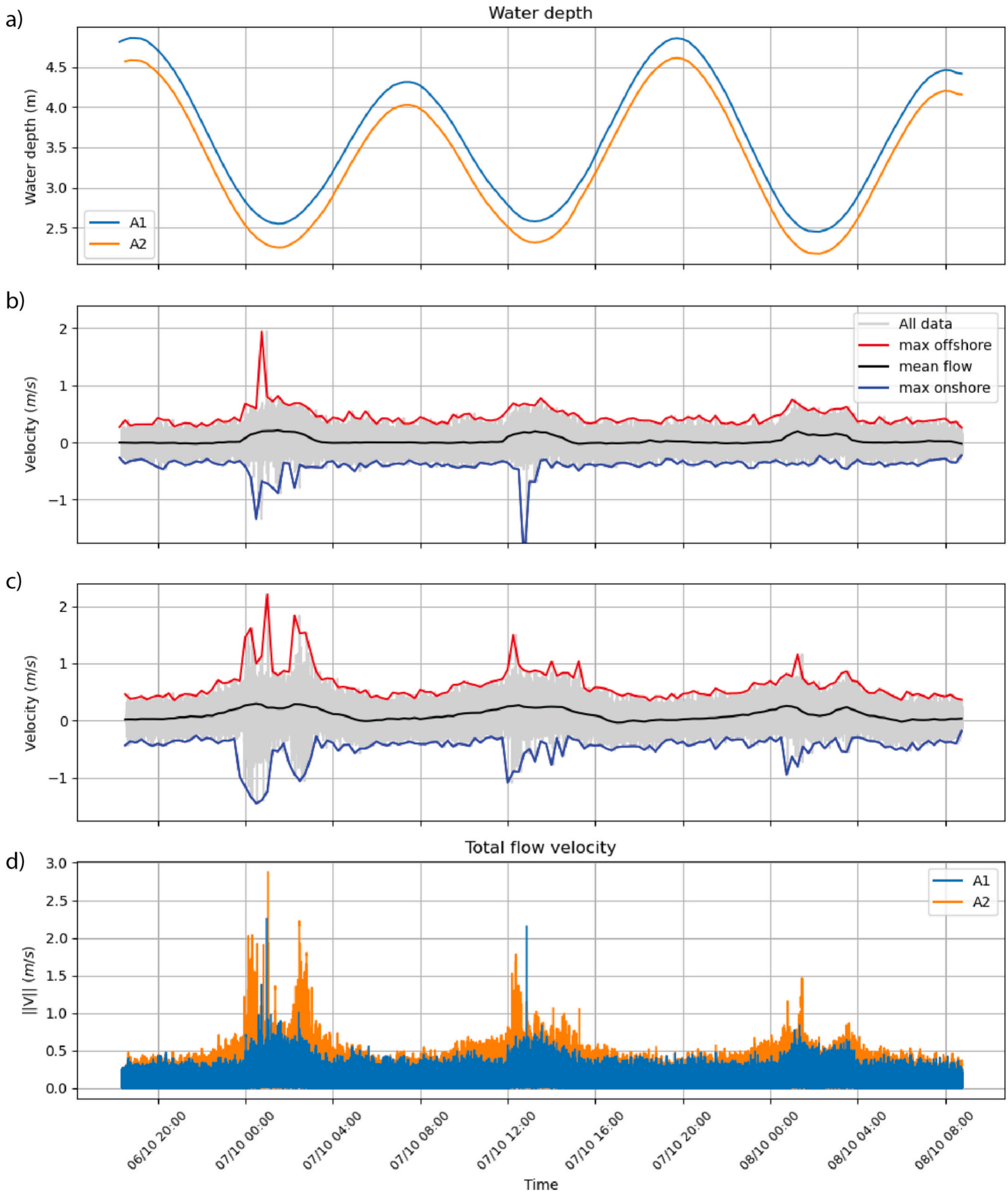

Fig. 7. Field measurements of (a) water depths measured at instruments A1 and A2, (b) cross-shore current direction (offshore is positive) at instrument A1 and (c) at instrument A2. (d) shows the absolute magnitude of the current recorded at instrument A1 (orange) and A2 (blue).

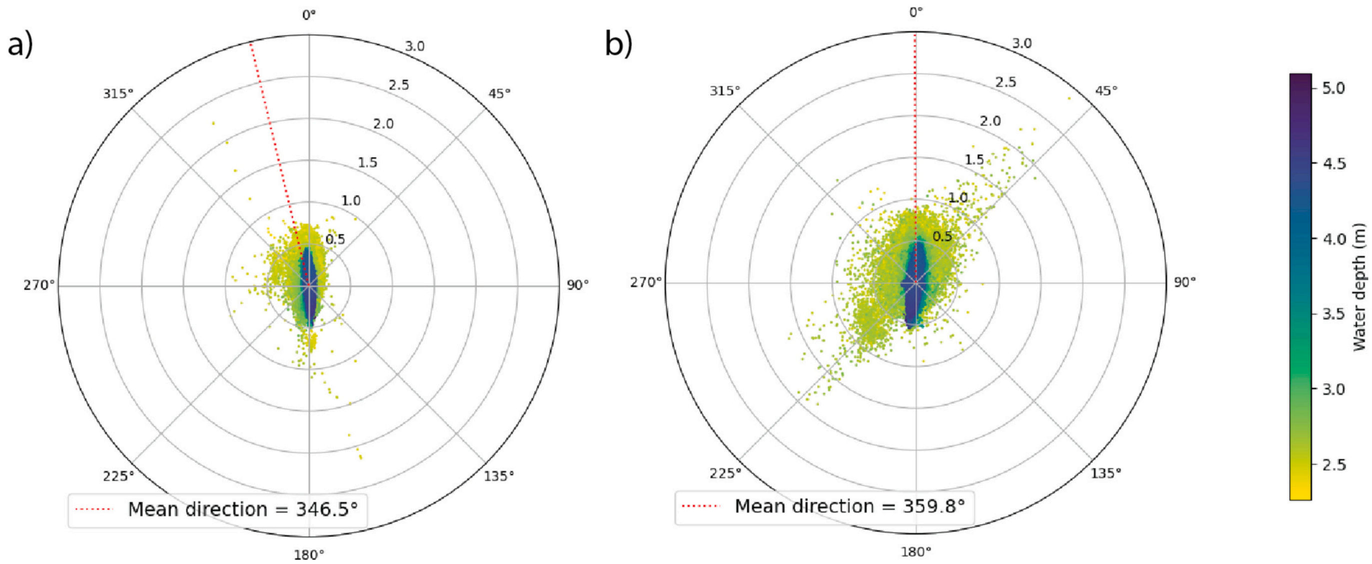

Fig. 8. a) Magnitude and direction of current velocity at instruments A1 and b) A2 during the deployment period. Mean current direction is shown with a red dashed line. Water depth is shown with a colour bar.

flux to more conclusively link lagoon outflow with sediment transport.

4.3. *Mechanistic interpretation of spur formation under observed current regimes*

Wave and current measurements in the forereef groove align with the hydrodynamics expected for the long, protected groove classification (Duce et al., 2020), with higher instantaneous current velocity in the upper groove and offshore-directed current throughout the tidal cycle. These conditions, measured for the first time on the GBR in this study, closely aligned with the mechanisms of reef platform development under low wave energy (Duce et al., 2020). The constant outflow of nutrient-rich lagoon water would foster coral growth on the upper forereef.

Additionally, given the high instantaneous offshore velocities (Fig. 7), we hypothesise that the current in the groove transports sediments offshore, fostering long-term spur development. Offshore currents were strongest near the reef crest (A2, Fig. 7) and decreased seaward (A1, Fig. 7), a pattern that supports the offshore transport and deposition of sediments. The ecological functioning of this process likely depends on current magnitude: when velocities remain within a moderate range, transported rubble and sediment can settle close enough to the spur-and-groove structure to facilitate colonisation and reef accretion. Conversely, if offshore currents become too strong, substrate may be carried beyond ecologically functional distances from the reef, reducing its potential to contribute to seaward reef growth. At Lizard Reef in the Central GBR, it was found that offshore currents, in the absence of extreme waves, transport 1.87 kg/yr of coral rubble offshore (Hughes, 1999). They proposed that this transport supports the seaward accretion of the forereef by providing an offshore substrate for corals to grow. Other studies at Looe Key Reef, Florida, (Shinn et al., 1982) and Ryukyu Island, Japan (Kan et al., 1995) have demonstrated spur development over consolidated carbonate reef sands. Evidence from U-Th dated cores taken from the forereef 560 m west of our study site reveals seaward lateral accretion of 231 m/ka on the reef flat and 24 m/ka on adjacent spurs (Duce et al., 2020). Similarly, cores have shown that reef flats have accreted seaward on the low-energy margins in OTR (Dechnik et al., 2016).

Although the dynamics of nutrients and sediments were not directly measured in this study, which focussed on groove hydrodynamics, our offshore currents align with Duce et al. (2020) *Mode 3* morphological model of SaG development, where lagoon outflow facilitates the seaward accretion of spurs and the reef flat in low-energy settings. Our findings provide the first hydrodynamic observations of a possible mechanism for this process, where offshore flow from the lagoon is focussed into grooves to support a constructional model of forereef development, driven by sediment accumulation and colonisation offshore of the reef crest.

Future research should examine the hydrodynamics of SaG systems across a range of reef exposures to better understand the current regimes that drive their development. In high-energy settings, where SaG features may be shaped by wave-driven erosion (Blanchon and Jones, 1997; Cloud Jr., 1954), strong wave forcing is thought to enhance sediment transport toward the lagoon, with currents converging within grooves (Duce et al., 2020). To resolve the mechanisms driving these processes, long-term deployments are required that capture the full vertical structure of currents across a range of hydrodynamic conditions. Complementary sediment trap deployments would help quantify the relative magnitude of sediment dynamics under these conditions (Storlazzi et al., 2011).

5. Conclusions

In this study, we present the first field measurements of currents at forereef spurs and grooves (SaG) from the Great Barrier Reef, providing critical insights into their hydrodynamics and role in reef development. The studied SaG exists under prevailing conditions of low-energy oblique incident waves. Our findings demonstrate that the hydrodynamics of low-energy SaGs are influenced by the outflow of lagoonal waters, generating consistent mean offshore currents in the upper forereef groove throughout the tidal cycle. This outflow, with maximum values of 2.05 m/s are driven by wave pumping (*i.e.*, larger waves on the opposite side of the reef push water into the lagoon generating an outflow on the low energy side), potentially transports sediment along the groove elongating the spurs and may contribute to the export of nutrients from the lagoon. These findings provide the first field-based support for the hypothesised Mode 3 of SaG development in the GBR, wherein lagoonal outflow sustains offshore groove currents and promotes the seaward accretion of spurs and the reef flat. This study highlights the importance of *in-situ* hydrodynamic measurements for understanding reef platform evolution and sets the stage for future long-term and multi-site investigations that would directly link sediment transport, deposition and reef accretion.

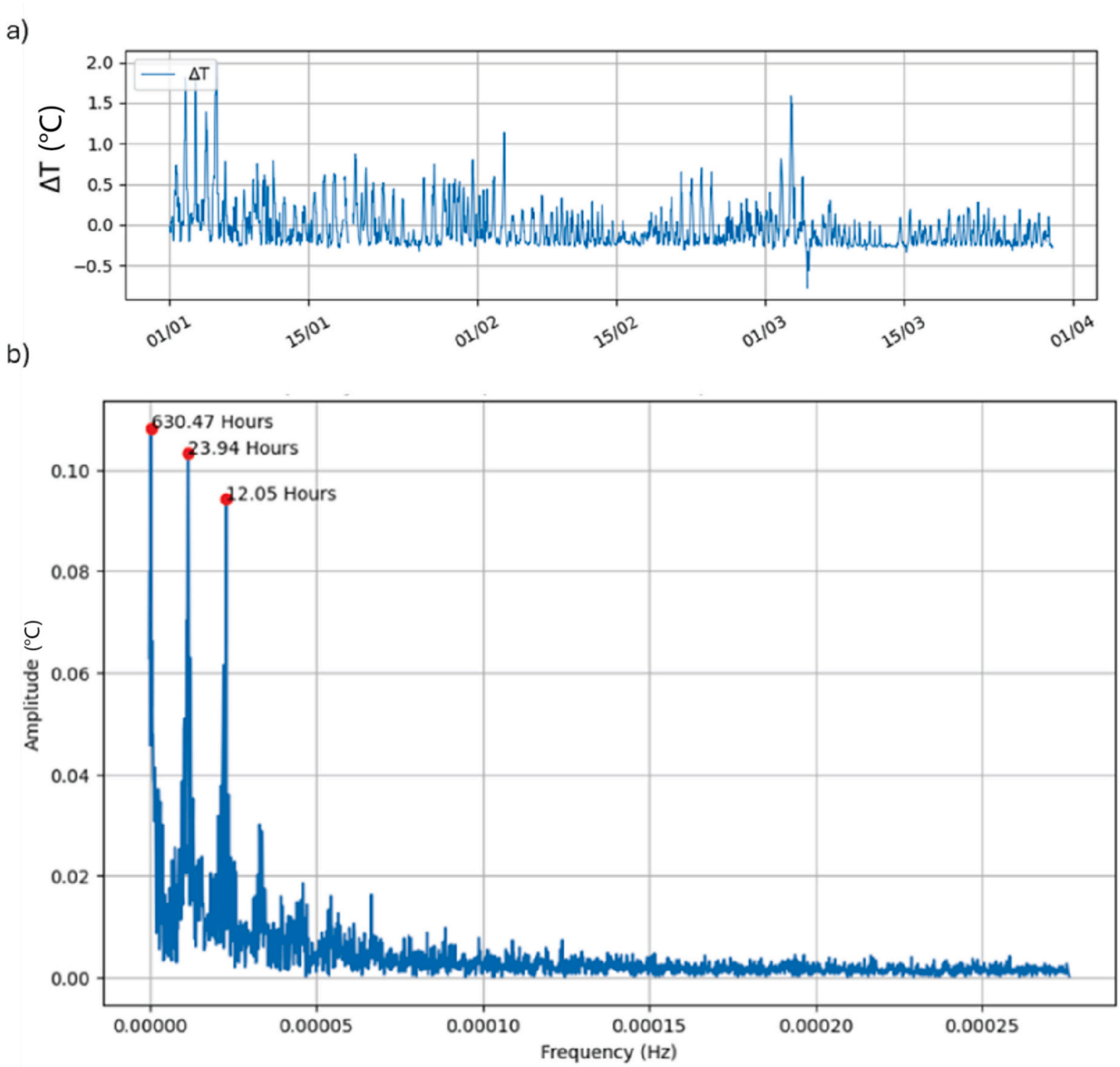

Fig. 9. (a) Temperature difference between surface and near-bed sensors at site B1. Negative values indicate thermal inversions, where bottom waters were warmer than surface waters. X-axis shows the date and month of records. (b) Amplitude frequency spectrum of temperature inversions at B1, highlighting dominant periodicities at 24 and 12 h (red points), consistent with diurnal and semi-diurnal tidal forcing.

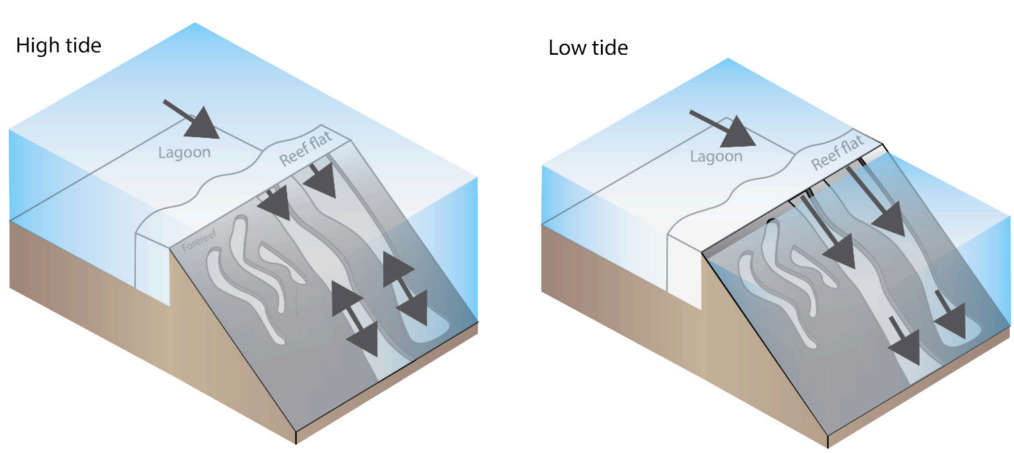

Fig. 10. Conceptual diagram of the mean current velocities from measured hydrodynamics in long-and-protected SaG at OTR (Fig. 3). Black arrows show current direction, and their length show relative current velocity in the grooves which is offshore for the full tidal cycle in the upper groove. Double headed arrows indicate no mean current and only wave induced oscillatory flow. The flow from the lagoon is always directed offshore.

Open research

Processed data from all instruments and Python based Jupyter Notebooks used in this analysis are available from Perris (2025).

CRediT authorship contribution statement

Lachlan Perris: Writing – review & editing, Writing – original draft, Visualization, Project administration, Methodology, Investigation, Formal analysis, Data curation, Conceptualization. **Tristan Salles:** Writing – review & editing, Software. **Thomas E. Fellowes:** Writing – review & editing, Project administration, Methodology. **Ana Paula Da Silva:** Writing – review & editing, Supervision, Conceptualization. **Stephanie Duce:** Writing – review & editing, Conceptualization. **Jody M. Webster:** Writing – review & editing, Resources, Project administration. **Alisha M. Thompson:** Writing – review & editing, Project administration. **Ana Vila-Concejo:** Writing – review & editing, Supervision, Resources, Project administration, Funding acquisition, Conceptualization.

Declaration of competing interest

The authors declare that they have no known competing financial interests or personal relationships that could have appeared to influence the work reported in this paper.

Acknowledgments

Lachlan Perris was supported by an RTP scholarship from The University of Sydney and the research was partially funded by Australian Research Council (ARC) Future Fellowship (FT100100215), ARC Discovery Program (DP220101125), and Geoscience Australia funding through the Marine Studies Institute at The University of Sydney. Field assistance provided by STEM students from Wenona School. Conceptual figure was produced with assistance by Tessa Chong.

Data availability

Research data and code is pubilshed with DOI:https://doi.org/10.5281/zenodo.17332298.

References

Acevedo-Ramirez, C.A., Stephenson, W., Wakes, S., Mariño-Tapia, I., 2021. Wave transformation on a fringing reef system with spur and groove structures. J Geophys Res Oceans 126, 1–14. https://doi.org/10.1029/2020JC016910.

Blanchon, P., Jones, B., 1997. Hurricane control on shelf-edge-reef architecture around Grand Cayman. Sedimentology 44, 479–506. https://doi.org/10.1046/j.1365-3091.1997.d01-32.x.

Byrne, M., Waller, A., Clements, M., Kelly, A.S., Kingsford, M.J., Liu, B., Reymond, C.E., Vila-Concejo, A., Webb, M., Whitton, K., Foo, S.A., 2025. Catastrophic bleaching in protected reefs of the Southern Great Barrier Reef. Limnol Oceanogr Lett. https://doi.org/10.1002/lol2.10456.

Callaghan, D.P., Nielsen, P., Cartwright, N., Gourlay, M.R., Baldock, T.E., 2006. Atoll lagoon flushing forced by waves. Coast. Eng. 53, 691–704. https://doi.org/10.1016/j.coastaleng.2006.02.006.

Cloud P.E., Jr., 1959. Geology of Saipan, Mariana Islands, part 4: submarine topography and shoal-water ecology. U. S. Geol. Surv. Prof. Pap. 361–445.

Cloud Jr., P.E., 1954. Superficial aspects of modern organic reefs. Sci. Mon. 79, 195–208.

da Silva, R.F., Storlazzi, C.D., Rogers, J.S., Reyns, J., McCall, R., 2020. Modelling three-dimensional flow over spur-and-groove morphology. Coral Reefs. https://doi.org/10.1007/s00338-020-02011-8.

Davies, P.J., 1983. Reef growth. In: Barnes, D.J. (Ed.), Perspectives on Coral Reefs. Clouston Publisher, Manuka, Australia, pp. 69–106.

Dean, R.G., Dalrymple, R.A., 1991. Water Wave Mechanics for Engineers and Scientists. In: Advanced Series on Ocean Engineering, 2nd ed, v. 2. World Scientific, Hackensack, NJ.

Dechnik, B., Webster, J.M., Nothdurft, L., Webb, G.E., Zhao, J. xin, Duce, S., Braga, J.C., Harris, D.L., Vila-Concejo, A., Puotinen, M., 2016. Influence of hydrodynamic energy on Holocene reef flat accretion, Great Barrier Reef. Quat. Res. (United States) 85, 44–53. https://doi.org/10.1016/j.yqres.2015.11.002.

Duce, S., Vila-Concejo, A., Hamylton, S., Bruce, E., Webster, J.M., 2014. Spur and groove distribution, morphology and relationship to relative wave exposure, Southern Great Barrier Reef, Australia. J. Coast. Res. 70, 115–120. https://doi.org/10.2112/si70-020.1.

Duce, S., Vila-Concejo, A., Hamylton, S.M., Webster, J.M., Bruce, E., Beaman, R.J., 2016. A morphometric assessment and classification of coral reef spur and groove morphology. Geomorphology 265, 68–83. https://doi.org/10.1016/j.geomorph.2016.04.018.

Duce, S., Dechnik, B., Webster, J.M., Hua, Q., Sadler, J., Webb, G.E., Nothdurft, L., Salas-Saavedra, M., Vila-Concejo, A., 2020. Mechanisms of spur and groove development and implications for reef platform evolution. Quat. Sci. Rev. 231. https://doi.org/10.1016/j.quascirev.2019.106155.

Duce, S., Mccarroll, R.J., Yiu, B., Perris, L.A., Yumba, B., Wales, S., Melbourne, E., 2021. Field measurements from contrasting reefs show spurs and grooves can dissipate more wave energy than the reef crest. Earth and Space Science Open Archive ESSOAr 413, 108365. https://doi.org/10.1016/j.geomorph.2022.108365.

Featherstone, W.E., Kirby, J.F., Hirt, C., Filmer, M.S., Claessens, S.J., Brown, N.J., Hu, G., Johnston, G.M., 2011. The AUSGeoid09 model of the Australian Height Datum. J. Geodyn. 85, 133–150. https://doi.org/10.1007/s00190-010-0422-2.

Frith, C.A., Mason, L.B., 1986. Modelling wind driven circulation One Tree Reef, Southern Great Barrier Reef. Coral Reefs 4, 201–211. https://doi.org/10.1007/BF00298078.

Gardner, J.P.A., Garton, D.W., Collen, J.D., 2011. Near-surface mixing and pronounced deep-water stratification in a compartmentalised, human-disturbed atoll lagoon system. Coral Reefs 30, 271–282. https://doi.org/10.1007/s00338-010-0701-7.

Goreau, T.F., 1959. The ecology of Jamaican coral reefs I. Species composition and zonation. Ecology 40, 67–90. https://doi.org/10.2307/1929924.

Goring, D.G., Nikora, V.I., 2002. Despiking acoustic Doppler velocimeter data. J. Hydraul. Eng. 128, 117–126. https://doi.org/10.1061/(asce)0733-9429(2002)128:1(117).

Grimaldi, C.M., Lowe, R.J., Benthuysen, J.A., Green, R.H., Reyns, J., Kernkamp, H., Gilmour, J., 2022. Wave and tidally driven flow dynamics within a coral reef atoll off Northwestern Australia. J Geophys Res Oceans 127. https://doi.org/10.1029/2021JC017583.

Harris, D.L., Vila-Concejo, A., Webster, J.M., Power, H.E., 2015. Spatial variations in wave transformation and sediment entrainment on a coral reef sand apron. Mar. Geol. 363, 220–229. https://doi.org/10.1016/j.margeo.2015.02.010.

Harris, D.L., Webster, J.M., Vila-concejo, A., Duce, S., Leon, J.X., 2023. Defining multi-scale surface roughness of a coral reef using a high-resolution LiDAR digital elevation model. Geomorphology 439, 108852. https://doi.org/10.1016/j.geomorph.2023.108852.

Hughes, T.P., 1999. Off-reef transport of coral fragments at Lizard Island, Australia. Mar. Geol. 157, 1–6. https://doi.org/10.1016/S0025-3227(98)00187-X.

Jell, J.S., Webb, G.E., 2012. Geology of Heron Island and adjacent reefs, great barrier reef, Australia. Episodes 35, 110–119. https://doi.org/10.18814/epiiugs/2012/v35i1/010.

Jost, C.H., Andréfouët, S., 2006. Long-term natural and human perturbations and current status of Clipperton Atoll, a remote island of the Eastern Pacific. Pac. Conserv. Biol. 12, 207–217. https://doi.org/10.1071/pc060207.

Kan, H., Hori, N., Nakashima, Y., Ichikawa, K., 1995. The evolution of narrow reef flats at high-latitude in the Ryukyu Islands. Coral Reefs 14, 123–130. https://doi.org/10.1007/BF00367229.

Karimpour, A., Chen, Q., 2017. Wind wave analysis in depth limited water using OCEANLYZ, a MATLAB toolbox. Comput. Geosci. 106, 181–189. https://doi.org/10.1016/j.cageo.2017.06.010.

Kinsela, M.A., Morris, B.D., Ingleton, T.C., Doyle, T.B., Sutherland, M.D., Doszpot, N.E., Miller, J.J., Holtznagel, S.F., Harley, M.D., Hanslow, D.J., 2024. Nearshore wave buoy data from southeastern Australia for coastal research and management. Sci. Data 11, 1–22. https://doi.org/10.1038/s41597-023-02865-x.

Klise, K., Pauly, R., Ruehl, K.M., Olson, S., Shippert, T., Morrell, Z., Bredin, S., Lansing, C., Macduff, M., Martin, T., Sivaraman, C., Gunawan, B., Driscoll, F., 2020. MHKiT (Marine and Hydrokinetic Toolkit) - Python. https://doi.org/10.5281/zenodo.3924683.

Lindhart, M., 2022. Loss of reef roughness increases residence time on an idealized coral reef. Sci. Rep. 12, 1–13. https://doi.org/10.1038/s41598-022-24045-4.

Lowe, R.J., Falter, J.L., 2015. Oceanic Forcing of Coral Reefs. Ann. Rev. Mar. Sci. 7, 43–66. https://doi.org/10.1146/annurev-marine-010814-015834.

Ludington, C.A., 1979. Tidal modifications and associated circulation in a platform reef lagoon. Mar. Freshw. Res. 30, 425–430. https://doi.org/10.1071/MF9790425.

MacMahan, J.H., Reniers, A.J.H.M., Thornton, E.B., Stanton, T.P., 2004. Infragravity rip current pulsations. J Geophys Res Oceans 109, 1–9. https://doi.org/10.1029/2003jc002068.

Monismith, S.G., 2007. Hydrodynamics of coral reefs. Annu. Rev. Fluid Mech. 39, 37–55. https://doi.org/10.1146/annurev.fluid.38.050304.092125.

Monismith, S.G., Herdman, L.M.M., Ahmerkamp, S., Hench, J.L., 2013. Wave transformation and wave-driven flow across a steep coral reef. J. Phys. Oceanogr. 43, 1356–1379. https://doi.org/10.1175/JPO-D-12-0164.1.

Munk, W.H., Sargent, M.C., 1948. Adjustment of Bikini Atoll to ocean waves. Trans. Am. Geophys. Union 29, 855. https://doi.org/10.1029/TR029i006p00855.

Odum, H.T., Odum, E.P., 1955. Trophic structure and productivity of a windward coral reef community on Eniwetok atoll. Ecological monographs 25, 291–320. https://doi.org/10.2307/1943285.

Perris, L., 2025. Current Flow in Low-Energy Coral Forereef Spurs and Grooves - Supporting Data and Notebooks. https://doi.org/10.5281/zenodo.17332298.

Perris, L., Salles, T., Fellowes, T., Duce, S., Webster, J.M., Vila-Concejo, A., 2023. The influence of coral reef spur and groove morphology on wave energy dissipation in contrasting reef environments. JGR Earth Surface 129, 27. https://doi.org/10.1029/2023JF007424.

Perris, L., Salles, T., Fellowes, T.E., Duce, S., Webster, J., Vila-Concejo, A., 2024. The influence of coral reef spur and groove morphology on wave energy dissipation in contrasting reef environments. Case Rep. Med. 129, 1–17. https://doi.org/10.1029/2023JF007424.

Ribal, A., Young, I.R., 2019. 33 years of globally calibrated wave height and wind speed data based on altimeter observations. Sci Data 6, 1–15. https://doi.org/10.1038/s41597-019-0083-9.

Rogers, J.S., Monismith, S.G., Feddersen, F., Storlazzi, C.D., 2013. Hydrodynamics of spur and groove formations on a coral reef. J Geophys Res Oceans 118, 3059–3073. https://doi.org/10.1002/jgrc.20225.

Rogers, J.S., Monismith, S.G., Dunbar, R.B., Koweek, D., 2015. Field observations of wave-driven circulation over spur and groove formations on a coral reef. J Geophys Res Oceans 145–160. https://doi.org/10.1002/2014JC010464. Received.

Rogers, J.S., Monismith, S.G., Koweek, D.A., Dunbar, R.B., 2016. Wave dynamics of a Pacific Atoll with high frictional effects. J Geophys Res Oceans 121, 350–367. https://doi.org/10.1002/2015JC011170.

Sartori, G., Boles, E.L., Monismith, S.G., Dunbar, R.B., Mumby, P.J., Khrizman, A., Capozzi, R., 2024. Morphologically driven sedimentation patterns on a coral reef. Coral Reefs. https://doi.org/10.1007/s00338-025-02629-6.

Sheppard, C., 1981. The groove and spur structures of Chagos atolls and their coral zonation. Estuar. Coast. Shelf Sci. 12, 549–560. https://doi.org/10.1016/S0302-3524(81)80081-3.

Shinn, E., 1963. Spur and groove formation on the Florida reef tract. SEPM Journal of Sedimentary Research 33, 291–303. https://doi.org/10.1306/74d70e34-2b21-11d7-8648000102c1865d.

Shinn, E.A., Hudson, J.H., Robbin, D.M., Lidz, B.H., 1982. Spurs and grooves revisited: construction versus erosion, Looe Key Reef, Florida. In: Proccedings of the Fourth International Coral Reef Symposium. Marine Sciences Center, University of the Philippines, Manila, pp. 475–483.

Silverman, J., Kline, D.I., Johnson, L., Rivlin, T., Schneider, K., Erez, J., Lazar, B., Caldeira, K., 2012. Carbon turnover rates in the One Tree Island reef: a 40-year perspective. J. Geophys. Res. Biogeosci. 117, 1–16. https://doi.org/10.1029/2012JG001974.

Smith, C., Vila-Concejo, A., Salles, T.B., 2020. Radwave: Python code for ocean surface wave analysis by satellite radar altimeter. J. Open Source Softw. 1, 46. https://doi.org/10.21105/joss.02083.

Smith, C., Vila-Concejo, A., Salles, T., 2023. Offshore wave climate of the Great Barrier Reef. Coral Reefs 42, 661–676. https://doi.org/10.1007/s00338-023-02377-5.

Sneh, A., Friedman, G.M., 1980. Spur and groove patterns on the reefs of the northern gulfs of the Red Sea. J. Sediment. Petrol. 50, 981–986. https://doi.org/10.1306/212F7B3F-2B24-11D7-8648000102C1865D.

Storlazzi, C.D., Logan, J.B., Field, M.E., 2003. Quantitative morphology of a fringing reef tract from high-resolution laser bathymetry: Southern Molokai, Hawaii. Bull. Geol. Soc. Am. 115, 1344–1355. https://doi.org/10.1130/B25200.1.

Storlazzi, C.D., Ogston, A.S., Bothner, M.H., Field, M.E., Presto, M.K., 2004. Wave-and tidally-driven flow and sediment flux across a fringing coral reef: Southern Molokai, Hawaii. Cont Shelf Res 24, 1397–1419. https://doi.org/10.1016/j.csr.2004.02.010.

Storlazzi, C.D., Field, M.E., Bothner, M.H., 2011. The use (and misuse) of sediment traps in coral reef environments: theory, observations, and suggested protocols. Coral Reefs 30, 23–38. https://doi.org/10.1007/s00338-010-0705-3.

Weydert, P., 1979. Direction de croissance des eperons sur le front d'un recif barriere - l'exemple du grand recif de tulear (madagascar). Mar. Geol. 30, M9–M19.

Wilson, P.R., 1985. Tidal studies in the One Tree Island lagoon. Mar. Freshw. Res. 36, 139–156. https://doi.org/10.1071/MF9850139.

Woolsey, E., Bainbridge, S.J., Kingsford, M.J., Byrne, M., 2012. Impacts of cyclone Hamish at One Tree Reef: integrating environmental and benthic habitat data. Mar. Biol. 159, 793–803. https://doi.org/10.1007/s00227-011-1855-8.

Zippenfenig, P., 2023. Open-Meteo.com Weather API. https://doi.org/10.5281/zenodo.7970649.